# Supergiant Elasticity and Fracture of 3D Spirally Wound MoS$_2$

Jianyang Wu,[1,2,*] Jianying He[2], Pilar Ariza[3], Michael Ortizd[4], and Zhiliang Zhang[2,*]

[1]Department of Physics, Research Institute for Biomimetics and Soft Matter, Jiujiang Research

Institute and Fujian Provincial Key Laboratory for Soft Functional Materials Research, Xiamen University,

Xiamen 361005, PR China

[2]NTNU Nanomechanical Lab, Norwegian University of Science and Technology (NTNU), Trondheim 7491,

Norway

[3]Escuela Técnica Superior de Ingenierkia, Universidad de Sevilla, Camino de los descubrimientos, s.n., 41092,

Sevilla, Spain

[4]Division of Engineering and Applied Science, California Institute of Technology, CA, 91125, Pasadena,

USA

**Abstract:** Recently experimentally synthesized three-dimensional (3D) MoS$_2$ spiral is a new kind of helical structure with technically robust properties. The knowledge about the mechanical properties of such appealing materials is indispensable but remains unexplored yet. Here, the stretching characteristics of 3D spirally wound MoS$_2$ as a new type of mechanical nanospring are explored by using large-scale molecular dynamic (MD) simulations. It is revealed that the MoS$_2$ spiral structures not only exhibit unique sawtooth-like tensile responses inaccessible from conventional springs, but also hold high stretching deformation capability. Surprisingly, there is a critical inner radius in jump of elasticity but not in the tensile strength; below which it yields elastic strain of less than 320%, while above which the elastic strain is over 1900%. The supergiant elasticity is primarily contributed by the sliding-reorientation action, stepwise opening and elastic deformation of nanoribbons of MoS$_2$ spirals. Moreover, imposed strain energy is mainly absorbed by the inner edges of MoS$_2$ spirals, and MoS$_2$ spirals catastrophically fail at the corner of inner hexagon-edge of buckled MoS$_2$ nanoribbons that are more stress-concentrated. This study provides important insights into facile design of MoS$_2$ spiral-based nanosprings with supergiant elongation capability for practical applications.

*Corresponding Emails: jianyang@xmu.edu.cn,zhiliang.zhang@ntnu.no

# 1. Introduction

Van der Waals (vdW) layered transition metal dichalcoginides (TMDCs), are a fascinating class of quantum structures for diverse applications, including optoelectronics, spintronics, valleytronics, catalysis and so on (Bhimanapati et al., 2015; Chhowalla et al., 2013; Gupta et al., 2015; Hu et al., 2018; Shearer et al., 2017; Zeng and Cui, 2015; Zhang et al., 2014). Those accessible promising applications mainly arise from their distinctive physical and chemical properties that can be finely tuned through thinning down from bulk to few-layer to monolayer, altering the structural phase and the stacking order of layers, alloying, hetero-structuring, mechanically straining, and so forth (Conley et al., 2013; Kang et al., 2013; Lee et al., 2010; Mak et al., 2010; Pan and Zhang, 2012; Pierucci et al., 2016; Puretzky et al., 2015; Voiry et al., 2015). As an example, as the thickness of vdW-layered $MoS_2$ is reduced from bulk to a monolayer, $MoS_2$ structure shows a transition from an indirect band gap ($E_g = 1.29$ eV) to a direct band gap ($E_g = 1.90$ eV), resulting in over $10^4$-fold enhancement in the photoluminescence (PL) quantum yield for monolayer $MoS_2$ (Lee et al., 2010; Mak et al., 2010; Splendiani et al., 2010). However, as a result of the weak light-matter interaction, arising from the atomic thickness of monolayer $MoS_2$, monolayer $MoS_2$ exhibits poor nonlinear optical conversion efficiency.(Zeng et al., 2015) To this end, thicker $MoS_2$ crystals with long interference length are required for highly efficient nonlinear optical applications.(Fan et al., 2017; Lin et al., 2018a; Lin et al., 2018b) Unfortunately, as a consequence of destructive interference of nonlinear polarization between the neighboring vdW-layers, multilayer $MoS_2$ crystals show vanishing oscillation of the second-harmonic generation effect with increasing numbers of layers, limiting its nonlinear optical applications (Li et al., 2013; Lin et al., 2018a; Lin et al., 2018b).

Recently, similar to three-dimensional (3D) graphene spirals with atomically thin helical periodicity (Šesták et al., 2015; Xu et al., 2016; Zhan et al., 2018; Zhan et al., 2017), 3D spirally wound $MoS_2$ nanostructures were achieved via the interfacial screw dislocation-driven growth mechanism (Kumar and Viswanath, 2016; Zhang et al., 2014). In contrast to monolayer $MoS_2$, 3D

spirally wound $MoS_2$ is able to yield larger effective conversion coefficients, and presents intriguing properties such as valley polarization and second order optical nonlinearity (Fan et al., 2017; Shearer et al., 2017; Zhang et al., 2014). Those unique properties are mainly attributed to spiral morphology of the $MoS_2$ nanostructures, and also that the spiral nanostructures are chiral and break the reflection and inversion symmetries of the lattices. More intriguingly, as a result of continuous covalent bonds in spirals made of vdW-layered $MoS_2$, remarkable enhancement in vertical conductivity (perpendicular to the layers) by carrying helical electrical current through the central threading dislocations can be realized (Ly et al., 2016), in sharp contrast to normal vdW-layered $MoS_2$ flakes. Those fascinating properties endow the spiral structure with appealing functionalities for diverse applications such as nanoscale optical, electronic and optoelectronics devices (Ly et al., 2016; Xu et al., 2016).

In those practical nanoengineering applications, despite valuable information of optical and electronic characteristics of 3D spirally wound $MoS_2$ has been reported (Ly et al., 2017; Ly et al., 2016; Shearer et al., 2017; Zhang et al., 2014), their mechanical behaviors are also critical for reliable and optimal performance of $MoS_2$ helicoid-based device systems and of interest to understand. However, to date, an overall picture of the tensile characteristics of 3D spirally wound $MoS_2$ remains poorly unknown. Therefore, in the present study, the nanomechanical characteristics including axial tension deformability and fracture of hexagon-shaped spiral $MoS_2$ with different dimensionality and inner spiral radii are explored by using large-scale classic MD simulations. This study provides valuable information for the future utilization and design of 3D $MoS_2$ nanosheets made of spirals in nanoscale molecular devices.

## 2. Models and Methodology

### 2.1 Atomic Models of $MoS_2$ spirals

Experimental characterizations revealed that 3D TMDCs spirals by screw-dislocation-driven growth mechanism show diverse polygonal projected morphology including triangular, hexagonal, or mixed shapes (Fan et al., 2018; Shearer et al., 2017). Similar to the case of coiled carbon nanotubes (CCNTs)(Wu et al., 2013a; Wu et al., 2013b; Wu et al., 2018b; Wu et al., 2018c), 3D spirally wound $MoS_2$ are constructed by a simple creation procedure proposed by (Liu et al., 2010) and (Zhan et al., 2017). Initially, columnar $MoS_2$ with periodicity in the off-plane direction is generated as shown in Figure 1a, where all layers are in AA stacking mode. Subsequently, 3D spirally wound $MoS_2$ is generated via identical screw dislocations with Burger's vector $\left|\vec{b}\right| = 6.141$ Å between neighboring $MoS_2$ nanoribbons, as seen in Figure 1b, where the magnitude of Burger's vector $\left|\vec{b}\right|$ is the thickness ($t$) of monolayer $MoS_2$ (Liang et al., 2009; Stewart and Spearot, 2013). The screw dislocation is achieved by intentionally bonding of interlayered Mo-S. In this study, 3D spirally wound $MoS_2$ with hexagon-shaped projection are specifically considered and taken into investigation. As it is seen in Figure 1, the hexagonal exterior is bounded by all-zigzag edges. It is noted that, due to the structural heterogeneity of $MoS_2$ crystal lattices, all-zigzag hexagonal edges in $MoS_2$ spirals are alternately S- and Mo-terminated. Moreover, the left-handed $MoS_2$ spirals are only studied in the present work, although an experimentally synthesized $MoS_2$ spiral shows identical probability between left- and right-handed helical confirmations (Shearer et al., 2017; Zhang et al., 2014). This is because, from the mechanical point of view, left- and right-handed spirals with identically coiled parameters and elemental compositions exhibit equal mechanical properties. Similar to graphene spirals (Zhan et al., 2017), a $MoS_2$ spiral structure is also mainly characterized by three geometrical parameters, including the outer radius $R$, inner radius $r$ and pitch distance $t$. Thus, the width of spiral $MoS_2$ is obtained as $w = R - r$. To ensure that the length of the spiral is over two times the Lennard-Jones (LJ) cutoff distance, all $MoS_2$ spirals composed of four complete coils along the helical axis are generated. A periodic boundary condition (PBC) is only imposed on the helical axis, while the perimeters of the

simulation boxes are free to simulate free-standing spiral $MoS_2$. Such hybrid application of PBC and non-PBC offers unconstrained ends to avoid any spurious end effects during the elongations.

## 2.2 MD simulations

Prior to MD simulations of axial loading, spiral $MoS_2$ are initially quasi-statically relaxed to a local minimum configuration by the conjugate gradient method with energy and force tolerances of $10^{-4}$ eV and $10^{-4}$ eV Å, respectively. Then, MD relaxation is carried out with $10^5$ timesteps to equilibrate the spirals. During the MD equilibrium process, the length of as-created spirals changes in the helical axis direction for reaching zero pressure under NPT (constant number of particles, pressure, and temperature) ensemble. The pressure and temperature are controlled by Nosé-Hoover barostat and Nosé-Hoover thermostat. Finally, uniaxial tension MD simulation of the relaxed spiral models under deformation-controlled technique is performed with a constant strain rate of $10^9$ s$^{-1}$under NVT (constant number of particles, volume, and temperature) ensemble with Nosé-Hoover thermostat. A small MD timestep of 0.2 fs with the velocity-Verlet algorithm is used to integrate the equation of atomic motions in the MD calculations. During the uniaxial MD tension, the spiral $MoS_2$ undergoes a Poisson's contraction in the transverse direction. The stretching force and stress are computed during the MD simulations from the virial stress tensor components on each atom. To eliminate the strong thermal fluctuations, a low temperature of 10 K is adopted in all MD simulations.

## 2.3 Forcefield for Modeling $MoS_2$ spirals

All the classic MD simulations are conducted using the Large-scale Atomic/Molecular Massively Parallel Simulator (LAMMPS)(Plimpton, 1995) package with a short-range many-body reactive empirical bond-order (REBO) potential plus a long-range two-body LJ potential (Liang et al., 2009). The REBO potential parameterized by (Liang et al., 2009) is capable of not only describing crystal properties but also dynamically capturing breaking and re-forming events of covalent bonds of $MoS_2$ systems (Stewart and Spearot, 2013; Wu et al., 2015). As suggested by (Wang et al., 2016), the

parameters of the original $MoS_2$-REBO potential were tuned to avoid artificial stiffening behavior. It has been shown that the modified $MoS_2$-REBO forefield is able to accurately predict the mechanical properties of $MoS_2$ nanostructures including their elastic and plastic behaviors (Wu et al., 2018a; Wu et al., 2019). In addition, for the non-bonded vdW interactions in the $MoS_2$ system, a LJ 12-6 potential for Mo-Mo, S-S and Mo-S interactions in the spiral $MoS_2$ system is adopted.

## 3. Results and Discussion

### 3.1 Structural Characteristics and Energetics in $MoS_2$ Spirals

Unlike vdW-layered $MoS_2$ crystals where there are no covalent bonds between interlayers, a $MoS_2$ spiral is structurally characterized by continuously covalent-bonded $MoS_2$ nanosheets as a result of the introduction of screw dislocations between neighboring layers. The introduction of screw dislocations in $MoS_2$ spirals could change the structural characteristics of vdW-layered $MoS_2$ nanosheets. Figures 2a and 2b show the top-viewed structural motifs of fully relaxed $MoS_2$ spirals with $R = 36.37$ Å, $r = 0.00$ Å and $R = 36.37$ Å, $r = 11.25$ Å, respectively. To discern the stacking characteristics in $MoS_2$ spirals, neighboring turns of $MoS_2$ spirals are alternately red- and blue-rendered. It is observed that the initial perfect AA stacking layers in both $MoS_2$ spirals are not preserved after structural relaxations. Instead, both $MoS_2$ spirals show complex layer stacking morphologies. As it is indicated by the hexagonal exterior edges, the non-uniformly relative rotational displacements between neighboring layers are mainly attributed to the complex stacking morphologies in both $MoS_2$ spirals. For the inner hole-free $MoS_2$ spiral, both common AA and AB stacking modes are detected from Figure 2a, which is in good agreement with previous experimental identifications.(Shearer et al., 2017; Zhang et al., 2014) However, the AA and AB stacking orders are heterogeneously distributed in the layers of inner hole-free $MoS_2$ spirals. The AA stacking order is mainly distributed in the center of the $MoS_2$ spiral. This is because the dislocation cores are located in the center of the $MoS_2$ spiral, which limits the displacement sliding of spiral layers. Besides, in addition to the normal AA and AB stacking modes, a new stacking is observed, which

stands in the middle states of AA and AB stacking orders. Such new stacking order was not observed by previous experimental characterizations. There are two main reasons for explaining the new stacking mode in the $MoS_2$ spiral. The first one is that, as a result of the application of PBC in the axial helical directions, our MD $MoS_2$ spirals are infinite long and thus the relative rotational displacements are more difficult to occur. However, the experimentally synthesized $MoS_2$ spirals are finite helical length and the half-exposed ends are more easily rotated to achieve energy-favorable stacking configurations. The other one is that experimentally synthesized $MoS_2$ spirals are over one order of magnitude larger than our MD models. A relative slight shift of adjacent spiral layers could result in AA or AB stacking order from the new stacking order. With regards to the $MoS_2$ spiral with hexagonal inner hole, it is found that the more energy-favorable AB stacking order becomes more pronounced, while the higher energy-penalty AA stacking motif almost vanishes. Such stacking transformation is due to that the delete of rigid region of dislocation core significantly frees the relative rotational movements of spiral layers, as indicated by the larger lattice mismatch between spiral layers from the exterior edges in Figure 2b. Likewise, the new stacking mode appears in the hollow $MoS_2$ spiral.

To understand the bond configurations in $MoS_2$ spirals, the bond lengths of polar Mo-S are computed. Figures 2c and 2d present the contours of bond length for both inner hole-free and hollow $MoS_2$ spirals, respectively. Apparently, both spirals show non-uniform distributions of bond length of Mo-S. Inner hole-free $MoS_2$ spiral show both large and small bond lengths of Mo-S and distortion of hexagonal rings in the central dislocation cores and. This indicates that, as a result of screw dislocations, the Mo-S bonds and Mo-S-Mo and S-Mo-S angles in the central dislocation core are either highly stretched or contracted. Moreover, the dangling bonds in the exterior edges are also contracted due to the surface effect, particularly for the S-terminated edges. As for the hollow $MoS_2$ spiral, contraction of Mo-S bonds is also observed in both interior and exterior edges. Instead, the second outermost Mo-S bonds adjacent to the Mo-terminated edges in both spirals are remarkably

strained. The lengths of Mo-S bonds in the interior of both spirals are relatively uniform and similar to the bulk counterpart of $MoS_2$ crystals. Those abovementioned structural characteristics are also found in other dimensional $MoS_2$ spirals.

In order to quantitatively uncover the effect of dimensionality on the bond configurations in spirals, the distribution profiles of Mo-S bond length in different inner hole-free and hollow $MoS_2$ spirals are calculated and shown in Figures 3a and 3b. Clearly, vdW-layered perfect $MoS_2$ crystal shows a narrow distribution of Mo-S bond and one peak at around 2.446 Å in the curve. The MD predicted bond length of Mo-S is slight larger than that by experimental measurements (2.420 Å) (Holinski and Gänsheimer, 1972). Unlike bulk $MoS_2$, wide distributions of bond length in the curves are observed for $MoS_2$ spirals. For inner hole-free $MoS_2$ spirals, as the radius ($R$) is decreased, a wider distribution of bond length appears as shown in Figure 3a. This is because of a large ratio of atoms located in the edges and dislocation cores to all atoms for small spirals. This indicates that changes in Mo-S configurations of small-sized spirals becomes more pronounced. Moreover, several peaks in the curves are identified. The peaks located at small abscissa positions correspond to the Mo-S bonds at the edges and dislocation cores, while the peak situated at large abscissa positions explains the large bond length of Mo-S in the dislocation cores and the second outermost structures. The highest peaks in the curves correspond to the Mo-S bonds in the interior of spirals. It is revealed that the length of those Mo-S bonds slightly deviate from 2.446 Å of bulk $MoS_2$ (Holinski and Gänsheimer, 1972). It is noted that those peaks can be also indicated by the Figure 2c. For the hollow $MoS_2$ spirals, similar characteristics in the distribution profiles of Mo-S bonds are observed.

Additionally, the hybrid stacking orders could influence the thickness of layers (pitch distance $t$) in the $MoS_2$ spirals. Figures 4a and 4c show the normalized thickness of layer of fully relaxed $MoS_2$ spirals ($t/t_{bulk}$) as a function of outer and inner radii ($R$ and $r$), respectively. Obviously, the pitch distance of $MoS_2$ spirals is strongly dependent on both outer and inner radii. The $MoS_2$ spiral shows a monotonic reduction in the pitch distance as either the outer or inner radius is enlarged. For

example, for inner hole-free MoS$_2$ spirals, the normalized pitch distance decreases by around 0.7% as the outer radius is increased from 12.42 Å to 36.37 Å. However, by examining the linear fitting slopes of the curves, it is found that change in the inner radius is more sensitive to the pitch distance. This indicates that the area of the dislocation core in the center of MoS$_2$ spirals plays a more important role in the pitch distance. As it is expected, the pitch distances of both inner hole-free and hollow MoS$_2$ spirals are larger than that of counterpart bulk MoS$_2$. This mainly comes from that, due to the screw dislocations, the AA and the new stacking orders in MoS$_2$ spirals enlarge the gap of neighboring layers. Figures 4b and 4d present the potential energy per atom as a function of the outer and inner radii $R$ and $r$, respectively. As it is seen, both potential energies of inner hole-free and hollow MoS$_2$ spirals show nonlinear relationships with the outer and inner radii ($R$ and $r$), resulting from the edge effects.

## 3.2 Tensile Characteristics of MoS$_2$ Spirals

Unlike vdW-layered MoS$_2$ nanosheets, mechanical behaviors of tightly wound MoS$_2$ spirals via screw dislocations are interesting for their practical nanoengineering applications. The effects of outer radius on the helical axial stretching behaviors are initially investigated. Figures 5a-d present the axial tensile stress - strain responses of inner hole-free MoS$_2$ spirals with the outer radius ranging from 12.42 to 36.37 Å. Apparently, all studied MoS$_2$ spirals show strong nonlinearity in the mechanically deformational curves, which is inaccessible for engineering mechanical springs that yield linear elastic responses under axial tension. In the initial small strain regimes, the stretching loads pronouncedly rise to maximum strengths as the elongation is enlarged to critical values. This deformation process is mainly against the vdW-adhesions between adjacent layers in MoS$_2$ spirals. The vdW forces governed initial tension stiffness of spirally wound MoS$_2$ can be determined from the linear fitting slopes of the stress-strain curves. It is calculated that the initial tensile stiffness are similar to the tightly wound coiled CNTs (Wu et al., 2013a; Wu et al., 2018c), but one order of magnitude lower than the in-plane stiffness of MoS$_2$ sheet (Wu et al., 2018a; Wu et al., 2019). This is

because the vdW-bonding forces are much weaker than the Mo-S covalent bonding forces. Moreover, the initial tensile stiffness depends on the dimensionality of $MoS_2$ spirals; $MoS_2$ spirals show a reduction trend in the initial tensile stiffness as the outer radius is increased. This is mainly explained by that, as the outer radius is decreased, the loading stress is mainly contributed by the covalent bonds located in the dislocation cores. Similarly, the maximum strength (peak stress) is also connected with the outer radius. As the outer radius is increased from 12.42 to 36.37 Å, the maximum strength is reduced by around 87.5%. Beyond the initial tension, stretching of multi-turns $MoS_2$ spirals produces mechanical curves with complex sawtooth-like patterns of peaks. Those peak loads are much lower than that of the initial peak. Those peaks distributed in the tensile curves suggest stepwise occurrences of multiple structural transformations during the elongation process. It is noted that the red arrows indicate the failure strains of the $MoS_2$ spiral. Finally, the mechanical loads suddenly drop to zero, reflecting the complete rupture of $MoS_2$ spirals. In contrast to the highest-peak stress and the initial tensile stiffness, $MoS_2$ spiral with larger outer radius shows higher rupture strain. Remarkably, $MoS_2$ spiral with outer radius of 36.37 Å is able to yield rupture strain of around 600%, showing outperforming deformational capacity.

To further reveal the deformation mechanisms underlying the behind complex nonlinear mechanical responses, the development of the atomic structure of spirally wound $MoS_2$ subjected to helical axial elongation is further examined. As an example, a series of snapshots of $MoS_2$ spiral with the largest outer radius at different critical strains are therefore captured and displayed in Figure 6, where the atoms are colored on the basis of $\sigma_{zz}$. In equilibrium ($\varepsilon = 0.00$), spirally wound $MoS_2$ shows uniform gap spacing (around 2.90 Å) between neighboring spring turns. As the tensile strain is applied from 0.00 to 0.54, $MoS_2$ spiral deforms mainly by uniform self-reorientation and collective sliding of the spiral nanoribbons, instead of enlargement of the inter-turn gap spacing. This indicates that the separation between nanoribbons of $MoS_2$ spiral is not capable of accommodating the low global axial deformation as a result of strong binding energy between the spiral nanoribbons, while

the imposed global strain energy are easily absorbed by the sliding and reorientation actions of $MoS_2$ nanoribbons. The tension stresses $\sigma_{zz}$ associated to Mo atoms grow with increasing global strain. Such deformation produces initially steep increase to the highest peak but is followed by strong oscillation in the loading stress. With further increasing the axial strain to a critical value, the deformation of the $MoS_2$ spiral is characterized by the development of bending-buckling and opening of the $MoS_2$ spiral, as it is seen in the spiral configuration at strain of 0.72 in the Figure 6. This implies that the sliding and reorientation behaviors no longer accommodate the further extension. Because of the buckling of multilayered nanoribbons, the spiral is locally compressed. Once the strain reaches to strain of 0.76, one turn of the $MoS_2$ spiral spring is completely opened with a big gap spacing and the buckled nanoribbons recover to flat configurations, resulting in significant release of atomic stresses. The opening of the $MoS_2$ spiral therefore gives rise to a deep drop of the global loading stress to around 0.76 GPa. Note that, during this complex deformation, no bond-formation and -breaking occur. As the axial strain is enlarged to about 1.28, the $MoS_2$ spiral elastically deforms by enlargement of the gap spacing between opened spiral coils. Meanwhile, the atomic stresses $\sigma_{zz}$ in the inner of $MoS_2$ spiral are augmented with increasing strain, resulting in the re-increase in the global loading stress. As further elongation is applied, inner edges become highly localized stress concentrated and the global pulling stress is not able to peel off the neighboring vdW-bonding nanoribbons. Instead, $MoS_2$ spiral deforms by catastrophic failure via the dissociation of Mo-S covalent bonds in the inner hexagonal corner, resulting in sudden drop of loading stress as indicated by the red arrow in Figure 4d. This deformational mechanism strikingly differs from the cases of graphene spirals and tightly wound coiled CNTs where elastically stepwise separations of all spiral coils under high elongations are identified (Wu et al., 2013a; Wu et al., 2018c; Zhan et al., 2017). The fracture propagates along the zigzag direction of nanoribbon and terminates to form a nanohinge-like configuration. Subsequently, the pulling force peels off another piece of nanoribbon because the global loading force is located at the exterior edge for confronting the vdW-adhesions.

Afterwards, the global pulling stress is switched to the inner edge, resulting in another zigzag-directional fracture in the exposed nanoribbon, as displayed by the configuration at strain of 5.17. As the elongation is enlarged from strain of 5.17 to 5.97, the residual spiral coils reorient themselves in a direction 90° from the global deformation axis with high shear stresses. Such deformation mechanism gives rise to increase in the global loading stress as seen in Figure 4d. Finally, dissociation of Mo-S bonds at one nanohinge occurs, leading to complete rupture of the $MoS_2$ spirals. Note that the other three smaller $MoS_2$ spirals exhibit similar deformation mechanisms.

**3.3 Critical Inner Radius for Achieving Supergiant Deformability of $MoS_2$ Spirals**

Because the global pulling stress is highly concentrated on the inner edges, the opening of $MoS_2$ spiral nanoribbons by helical axial stretching is limited, resulting in low elasticity and ductility. Enlargement of the inner edges by removing the inner dislocation cores could enhance both, elasticity and stretchability. To this end, the effects of inner radius on the mechanical behaviors of $MoS_2$ spirals are examined. Figures 6a-i plot the tensile stress-strain diagrams of $MoS_2$ spirals with inner radius varying from 0.0 to 21.80 Å but identical outer radius of 36.37 Å. Obviously, the characteristics of the strong nonlinear loading curves are quite similar; the initially small deformation responses are primarily characterized by steep increase in loading stress followed by frequent oscillations of high loading stress, whereas for the posterior large deformation $MoS_2$ spirals show characteristic sawtooth-like patterns in the loading curves where low peaks stresses are observed. Moreover, it is revealed that both the highest peak stresses and stretching stresses in the long-range sawtooth-like regions are quite comparable, although the inner radii of those $MoS_2$ spirals are very different. This implies that the inner radius is not critical to the pulling stress for elongation. However, $MoS_2$ spiral shows pronounced enhancement in the rupture strain with increasing the inner radius. As an example, as the inner radius is enlarged from 0.0 to 21.80 Å, the rupture strain of $MoS_2$ spiral is enhanced by around 480%. Intriguingly, the elasticity is surprisingly enhanced by about 2500% as illustrated by the arrows that indicate the initial fracture strains. It is also revealed that

there is a sudden change in the elasticity of $MoS_2$ spirals as the inner radius is slightly enlarged from 11.25 to 14.11 Å. $MoS_2$ spiral with inner radius of 11.25 Å yields elastic strain of around 310%, whereas for the one with 14.11 Å it is able to exhibit supergiant elastic strain of 1900%. This clearly indicates that there are very different elastic deformation scenarios between $MoS_2$ spiral with small and large inner radii.

To figure out the deformation mechanisms underlying the inner radius dependent stretchability of the $MoS_2$ spirals, the evolution of molecular configurations of hollow $MoS_2$ spirals under helical axial tension is examined. Similarly, as an example, a number of snapshots of deformational configurations of $MoS_2$ spiral with inner radius of 14.11 Å at different critical tension strains from MD simulations are captured and displayed in Figure 7 to reveal the supergiant elasticity and stretchability, where the color code of atoms is on the basis of stretching stress $\sigma_{zz}$. Similar to the cases of other $MoS_2$ spirals, in the initial tensile deformation, the pulling of the $MoS_2$ spirals is dominated by the sliding-reorientation-buckling deformation mechanisms that give rise to the initial frequent variations of stretching stress in the loading curves. However, because $MoS_2$ spirals with larger inner radius is able to reorient their nanoribbons in larger direction angles and more shrink of inner radius of $MoS_2$ nanoribbon coils along the planes, significantly higher global axial deformation can be accommodated as indicated by the configurations at strains of 0.54 and 2.00 in Figures 6 and 7, respectively. This explains the larger elastic regions with frequent oscillation in pulling stress in the initial deformation. Moreover, reoriented $MoS_2$ nanoribbon coils with large inner radius are more highly uniform stress-concentrated. Remarkably, the following supergiant elastic deformation is primarily characterized by a series of sliding-buckling-opening mechanisms, in sharp contrast to the cases of $MoS_2$ spirals with inner radius varying from 0.0 to 11.25 Å where the late-stage elasticity are only contributed by elastically stretching opened nanoribbon. Finally, all the nanoribbon coils in the $MoS_2$ spiral are completely opened for accommodating supergiant elongation. Instead, the opened $MoS_2$ nanoribbons are non-uniformly distributed along the spiral axis. Specifically, a part of

opened nanoribbon is highly buckled without coiled morphology. This differs from the traditional spring coils and grapheme spirals whose opened coils are uniformly distributed along the helical axis. Unlike the strain-induced opening of coils of $MoS_2$ spiral, stretching of the fully opened $MoS_2$ spiral gives rise to significant increase in the loading stresses, as indicated in Figure 6. This signifies that deforming covalent bonds of Mo-S is more effectively absorb the stretch energy than that of stepwise opening of coils in $MoS_2$ spirals. Because of the bending buckling morphology, the nanoribbon shows complexity in stress states. For example, both inner and outer edges show positive stress, while the concave buckled surface is highly compressed. For other parts of the $MoS_2$ spiral, the inner edges of opened nanoribbon coils are tensiled, where for the middle regions of the coiled nanoribbons they are compressed. In comparison, it is revealed that the magnitude of tensile stress in the inner edges of buckled nanoribbon is higher than that of coiled nanoribbons. As a result, highly elongated $MoS_2$ spiral fails by dissociation of Mo-S bonds located at the inner edges of buckled nanoribbon as excess stretching is applied. This corresponds to the sudden drop of loading stress after the peak marked by the arrows in Figures 6f-i. Similar to the case of $MoS_2$ spiral with inner radius of 0.0 Å as shown in Figure 5, break-vs-arrest behavior of Mo-S bonds situated at the buckled nanoribbon dominates the plastic deformation. Finally, supergiant-elongation-at-rupture of $MoS_2$ spiral with inner radius of 14.11 Å is achieved, as illustrated by the configuration at strain of 21.67.

## 4. Conclusions

A new 3D helical structure of $MoS_2$ spiral has recently entered into the palette of promising building blocks for the next generation of smart devices and multifunctional materials due to its unique optical and electronic properties. This study mainly focuses on the role of outer and inner radius on the stretching characteristics of experimentally realized 3D $MoS_2$ spiral structures by using classic MD simulations based on a reliable many-body REBO combined with a two-body 12-6 LJ potentials. $MoS_2$ spirals show both outer and inner radii dependence in pitch distance, and their pitch distances exceed the interlayer gap spacing of bulk $MoS_2$ crystal. Such structural characteristics are mainly

attributed by the presence of screw dislocations that introduce complex hybrid stacking orders between nanoribbons of $MoS_2$ spirals. Moreover, as a result of the central dislocation cores, atomic structures in the central region are highly distorted and thus prestress-concentrated. All the investigated $MoS_2$ spirals exhibit characteristic sawtooth-like patterns in the tensile stress-strain curves. The initial frequent oscillation in loading stresses is mainly attributed to the sliding-reorientation-buckling mechanisms. For non-hollow $MoS_2$ spirals, dimensionality (outer radius) dependent mechanical properties including the initial tensile stiffness, maximum tensile strength, elasticity and ductility are revealed. However, with regard to the hollow $MoS_2$ spirals, it is unexpectedly identified a critical inner radius that dictates their elastic capacity. For example, when the inner radius of $MoS_2$ spiral is slightly enlarged from 11.25 to 14.11 Å, the elastic strain jumps from around 310% - 1900%. More importantly, the loading strength is almost not degraded. By analyzing their deformational configurations, it is revealed that the origin of this sudden change in elasticity is because coiled nanoribbons of $MoS_2$ spiral with inner radius of 14.11 Å are fully elastically opened for accommodating global axial elongation, whereas for those with inner radius of 11.25 Å, only one coiled nanoribbon is opened. Intriguingly, all opened coiled nanoribbons are non-uniformly distributed along the helical axis because one coiled nanoribbon is severely buckled with more stress concentration at the inner edge. A series of break-vs-arrest processes occur at the inner hexagon corner of the buckled nanoribbon. The fractures propagate along the zigzag direction of nanoribbons. These findings provide useful insights into the design of $MoS_2$-based nanosprings with outperforming elasticity for practical applications in device systems with coupling to their other properties.

**Acknowledgments**

## References

Bhimanapati, G.R., Lin, Z., Meunier, V., Jung, Y., Cha, J., Das, S., Xiao, D., Son, Y., Strano, M.S., Cooper, V.R., Liang, L., Louie, S.G., Ringe, E., Zhou, W., Kim, S.S., Naik, R.R., Sumpter, B.G., Terrones, H., Xia, F., Wang, Y., Zhu, J., Akinwande, D., Alem, N., Schuller, J.A., Schaak, R.E., Terrones, M., Robinson, J.A., 2015. Recent Advances in Two-Dimensional Materials beyond Graphene. ACS Nano 9, 11509-11539.

Chhowalla, M., Shin, H.S., Eda, G., Li, L.-J., Loh, K.P., Zhang, H., 2013. The chemistry of two-dimensional layered transition metal dichalcogenide nanosheets. Nature Chemistry 5, 263.

Conley, H.J., Wang, B., Ziegler, J.I., Haglund, R.F., Pantelides, S.T., Bolotin, K.I., 2013. Bandgap Engineering of Strained Monolayer and Bilayer MoS2. Nano Letters 13, 3626-3630.

Fan, X., Jiang, Y., Zhuang, X., Liu, H., Xu, T., Zheng, W., Fan, P., Li, H., Wu, X., Zhu, X., Zhang, Q., Zhou, H., Hu, W., Wang, X., Sun, L., Duan, X., Pan, A., 2017. Broken Symmetry Induced Strong Nonlinear Optical Effects in Spiral WS2 Nanosheets. ACS Nano 11, 4892-4898.

Fan, X., Zhao, Y., Zheng, W., Li, H., Wu, X., Hu, X., Zhang, X., Zhu, X., Zhang, Q., Wang, X., Yang, B., Chen, J., Jin, S., Pan, A., 2018. Controllable Growth and Formation Mechanisms of Dislocated WS2 Spirals. Nano Letters 18, 3885-3892.

Gupta, A., Sakthivel, T., Seal, S., 2015. Recent development in 2D materials beyond graphene. Progress in Materials Science 73, 44-126.

Holinski, R., Gänsheimer, J., 1972. A study of the lubricating mechanism of molybdenum disulfide. Wear 19, 329-342.

Hu, Z., Wu, Z., Han, C., He, J., Ni, Z., Chen, W., 2018. Two-dimensional transition metal dichalcogenides: interface and defect engineering. Chemical Society Reviews 47, 3100-3128.

Kang, J., Li, J., Li, S.-S., Xia, J.-B., Wang, L.-W., 2013. Electronic Structural Moiré Pattern Effects on MoS2/MoSe2 2D Heterostructures. Nano Letters 13, 5485-5490.

Kumar, P., Viswanath, B., 2016. Effect of Sulfur Evaporation Rate on Screw Dislocation Driven Growth of MoS2 with High Atomic Step Density. Crystal Growth & Design 16, 7145-7154.

Lee, C., Yan, H., Brus, L.E., Heinz, T.F., Hone, J., Ryu, S., 2010. Anomalous Lattice Vibrations of Single- and Few-Layer MoS2. ACS Nano 4, 2695-2700.

Li, Y., Rao, Y., Mak, K.F., You, Y., Wang, S., Dean, C.R., Heinz, T.F., 2013. Probing Symmetry Properties of Few-Layer MoS2 and h-BN by Optical Second-Harmonic Generation. Nano Letters 13, 3329-3333.

Liang, T., Phillpot, S.R., Sinnott, S.B., 2009. Parametrization of a reactive many-body potential for Mo--S systems. Physical Review B 79, 245110.

Lin, X., Liu, Y., Wang, K., Liu, X., Yan, Y., Li, Y.J., Yao, J., Zhao, Y.S., 2018a. Hybrid Three-Dimensional Spiral WSe2 Plasmonic Structures for Highly Efficient Second-Order Nonlinear Parametric Processes. Research 2018, 8.

Lin, X., Liu, Y., Wang, K., Wei, C., Zhang, W., Yan, Y., Li, Y.J., Yao, J., Zhao, Y.S., 2018b. Two-Dimensional Pyramid-like WS2 Layered Structures for Highly Efficient Edge Second-Harmonic Generation. ACS Nano 12, 689-696.

Liu, L.Z., Gao, H.L., Zhao, J.J., Lu, J.P., 2010. Superelasticity of Carbon Nanocoils from Atomistic Quantum Simulations. Nanoscale Research Letters 5, 478.

Ly, T.H., Kim, H., Thi, Q.H., Lau, S.P., Zhao, J., 2017. Superior Dielectric Screening in Two-Dimensional MoS2 Spirals. ACS Applied Materials & Interfaces 9, 37941-37946.

Ly, T.H., Zhao, J., Kim, H., Han, G.H., Nam, H., Lee, Y.H., 2016. Vertically Conductive MoS2 Spiral Pyramid. Advanced Materials 28, 7723-7728.

Mak, K.F., Lee, C., Hone, J., Shan, J., Heinz, T.F., 2010. Atomically Thin ${\mathrm{MoS}}_{2}$: A New Direct-Gap Semiconductor. Physical Review Letters 105, 136805.

Pan, H., Zhang, Y.-W., 2012. Tuning the Electronic and Magnetic Properties of MoS2 Nanoribbons by Strain Engineering. The Journal of Physical Chemistry C 116, 11752-11757.

Pierucci, D., Henck, H., Avila, J., Balan, A., Naylor, C.H., Patriarche, G., Dappe, Y.J., Silly, M.G., Sirotti, F., Johnson, A.T.C., Asensio, M.C., Ouerghi, A., 2016. Band Alignment and Minigaps in Monolayer MoS2-Graphene van der Waals Heterostructures. Nano Letters 16, 4054-4061.

Plimpton, S., 1995. Fast Parallel Algorithms for Short-Range Molecular Dynamics. Journal of Computational Physics 117, 1-19.

Puretzky, A.A., Liang, L., Li, X., Xiao, K., Wang, K., Mahjouri-Samani, M., Basile, L., Idrobo, J.C., Sumpter, B.G., Meunier, V., Geohegan, D.B., 2015. Low-Frequency Raman Fingerprints of Two-Dimensional Metal Dichalcogenide Layer Stacking Configurations. ACS Nano 9, 6333-6342.

Šesták, P., Wu, J., He, J., Pokluda, J., Zhang, Z., 2015. Extraordinary deformation capacity of smallest carbohelicene springs. Physical Chemistry Chemical Physics 17, 18684-18690.

Shearer, M.J., Samad, L., Zhang, Y., Zhao, Y., Puretzky, A., Eliceiri, K.W., Wright, J.C., Hamers, R.J., Jin, S., 2017. Complex and Noncentrosymmetric Stacking of Layered Metal Dichalcogenide Materials Created by Screw Dislocations. Journal of the American Chemical Society 139, 3496-3504.

Splendiani, A., Sun, L., Zhang, Y., Li, T., Kim, J., Chim, C.-Y., Galli, G., Wang, F., 2010. Emerging Photoluminescence in Monolayer MoS2. Nano Letters 10, 1271-1275.

Stewart, J.A., Spearot, D.E., 2013. Atomistic simulations of nanoindentation on the basal plane of crystalline molybdenum disulfide (MoS2). Modelling and Simulation in Materials Science and Engineering 21, 045003.

Voiry, D., Mohite, A., Chhowalla, M., 2015. Phase engineering of transition metal dichalcogenides. Chemical Society Reviews 44, 2702-2712.

Wang, S., Qin, Z., Jung, G.S., Martin-Martinez, F.J., Zhang, K., Buehler, M.J., Warner, J.H., 2016. Atomically Sharp Crack Tips in Monolayer MoS2 and Their Enhanced Toughness by Vacancy Defects. ACS Nano 10, 9831-9839.

Wu, J., Cao, P., Zhang, Z., Ning, F., Zheng, S.-s., He, J., Zhang, Z., 2018a. Grain-Size-Controlled Mechanical Properties of Polycrystalline Monolayer MoS2. Nano Letters 18, 1543-1552.

Wu, J., Gong, H., Zhang, Z., He, J., Ariza, P., Ortiz, M., Zhang, Z., 2019. Topology and polarity of dislocation cores dictate the mechanical strength of monolayer MoS2. Applied Materials Today 15, 34-42.

Wu, J., He, J., Odegard, G.M., Nagao, S., Zheng, Q., Zhang, Z., 2013a. Giant Stretchability and Reversibility of Tightly Wound Helical Carbon Nanotubes. Journal of the American Chemical Society 135, 13775-13785.

Wu, J., Nagao, S., He, J., Zhang, Z., 2013b. Nanohinge-Induced Plasticity of Helical Carbon Nanotubes. Small 9, 3561-3566.

Wu, J., Nie, G., Xu, J., He, J., Xu, Q., Zhang, Z., 2015. Structural instability and mechanical properties of MoS2 toroidal nanostructures. Physical Chemistry Chemical Physics 17, 32425-32435.

Wu, J., Shi, Q., Zhang, Z., Wu, H.-H., Wang, C., Ning, F., Xiao, S., He, J., Zhang, Z., 2018b. Nature-inspired entwined coiled carbon mechanical metamaterials: molecular dynamics simulations. Nanoscale 10, 15641-15653.

Wu, J., Zhao, H., Liu, J., Zhang, Z., Ning, F., Liu, Y., 2018c. Nanotube-chirality-controlled tensile characteristics in coiled carbon metastructures. Carbon 133, 335-349.

Xu, F., Yu, H., Sadrzadeh, A., Yakobson, B.I., 2016. Riemann Surfaces of Carbon as Graphene Nanosolenoids. Nano Letters 16, 34-39.

Zeng, H., Cui, X., 2015. An optical spectroscopic study on two-dimensional group-VI transition metal dichalcogenides. Chemical Society Reviews 44, 2629-2642.

Zeng, J., Yuan, M., Yuan, W., Dai, Q., Fan, H., Lan, S., Tie, S., 2015. Enhanced second harmonic generation of MoS2 layers on a thin gold film. Nanoscale 7, 13547-13553.

Zhan, H., Zhang, G., Yang, C., Gu, Y., 2018. Breakdown of Hooke's law at the nanoscale – 2D material-based nanosprings. Nanoscale 10, 18961-18968.

Zhan, H., Zhang, Y., Yang, C., Zhang, G., Gu, Y., 2017. Graphene helicoid as novel nanospring. Carbon 120, 258-264.

Zhang, L., Liu, K., Wong, A.B., Kim, J., Hong, X., Liu, C., Cao, T., Louie, S.G., Wang, F., Yang, P., 2014. Three-Dimensional Spirals of Atomic Layered MoS2. Nano Letters 14, 6418-6423.

**Figures and captions**
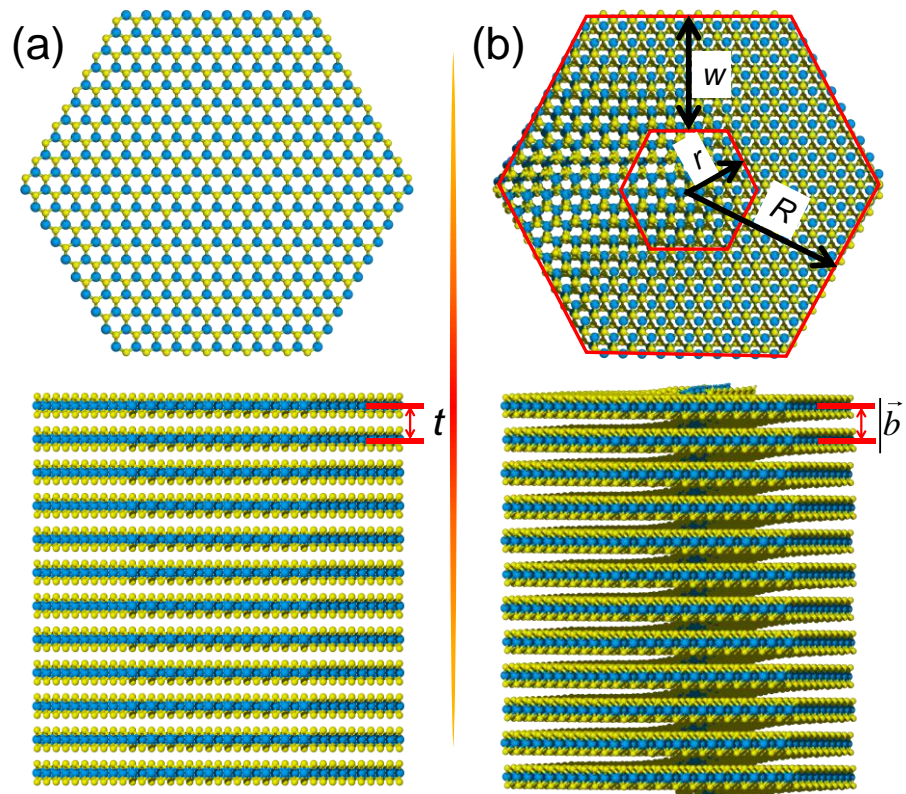


Figure 1. MoS$_2$ nanocoloum made of hexagon-shaped nanosheets. (a) Top- and side-viewed molecular structure of AA stacked MoS$_2$ nanocoloum. The red arrow indicates the interlayer gap spacing $t$ = 6.141 Å. (b) Top- and side-view of molecular structure of hexagon-shaped MoS$_2$ spiral constructed from screw dislocation. The three geometrical parameters including outer radius $R$, inner radius $r$ and width $w$ of nanoribbon of MoS$_2$ spiral are illustrated in the top-viewed image, while the burger's vector $\vec{b}$ of screw dislocation is marked in the bottom side-viewed image.
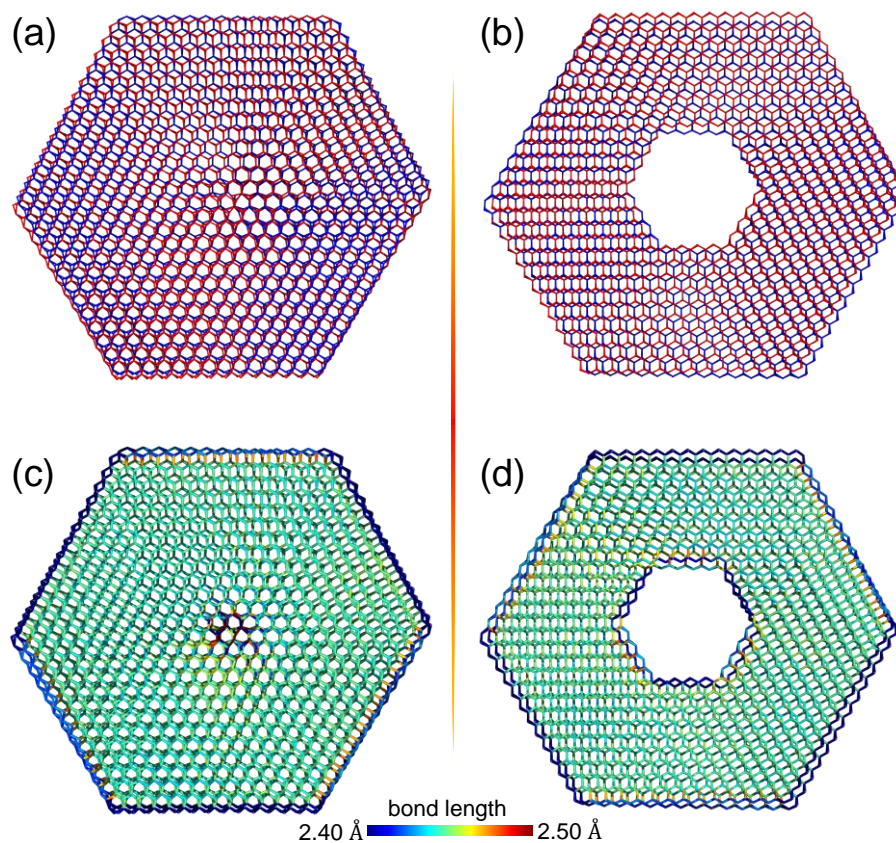
Figure 2. Structural characteristics of non-hollow and hollow $MoS_2$ spirals with outer radius of around 36.37 Å. (a) and (b) Top-viewed atomic structures of $MoS_2$ spirals with inner radius of 0.0 Å and 11.25 Å, respectively, where the coiled turns are alternately red- and blue-rendered for identification of stacking characteristics. (c) and (d) Top-views of atomic strucutres of $MoS_2$ spirals with inner radius of 0.0 Å and 11.25 Å, respectively, where the color code is on the basis of the bond length of Mo-S for distinguishing bond configurations.
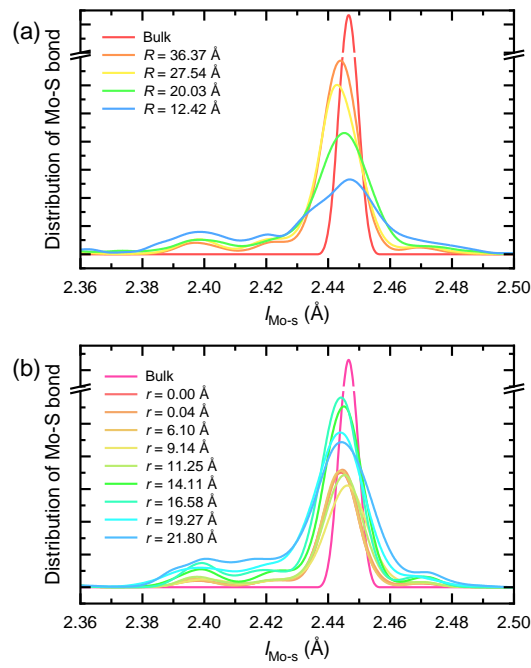
Figure 3. Geometry dependent distributions of Mo-S bonds in MoS$_2$ spirals. (a) Bond distribution profiles of Mo-S in non-hollow MoS$_2$ spirals with outer radius varying from 12.42 to 36.37 Å, as well the bulk MoS$_2$ crystal. (b) Comparison of bond distribution profiles of Mo-S in hollow MoS$_2$ spirals with inner radius in the range of 0.00 to 21.80 Å, as well the bulk MoS$_2$ crystal.
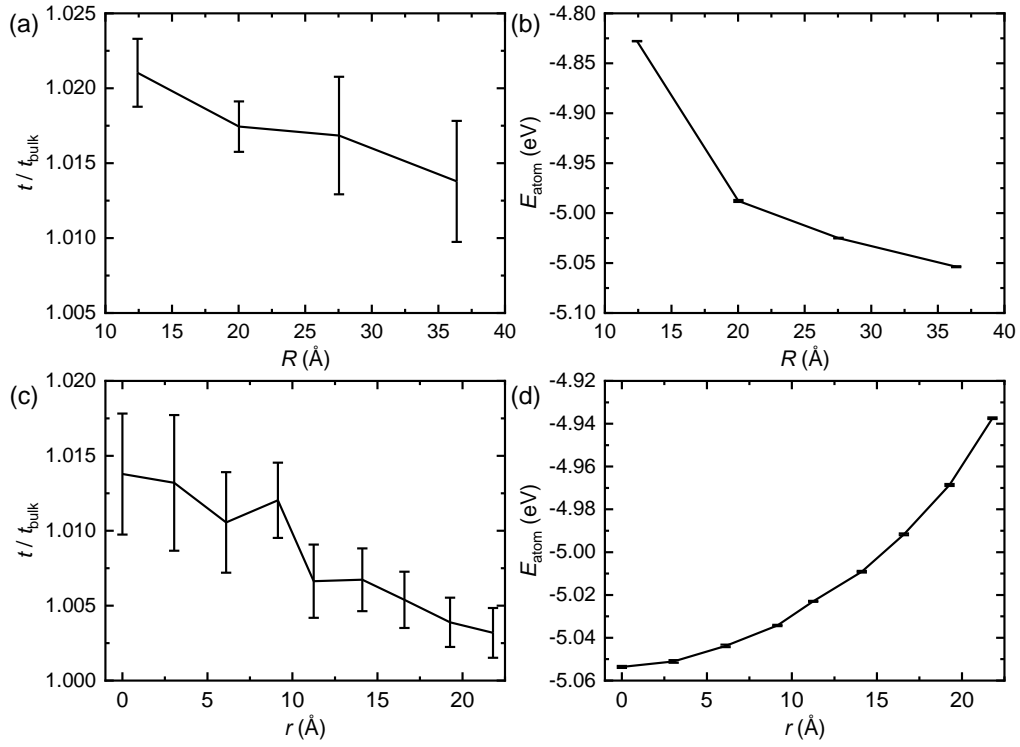
Figure 4. Geometry dependent pitch distance and energetics in MoS$_2$ spirals. (a) and (b) Normalized pitch distance and potential energy per atom in MoS$_2$ spirals with enlarging the outer radius from 12.42 to 36.37 Å. (b) Normalized pitch distance and potential energy per atom in MoS$_2$ spirals with increasing the inner radius from 0.00 to 21.80 Å.
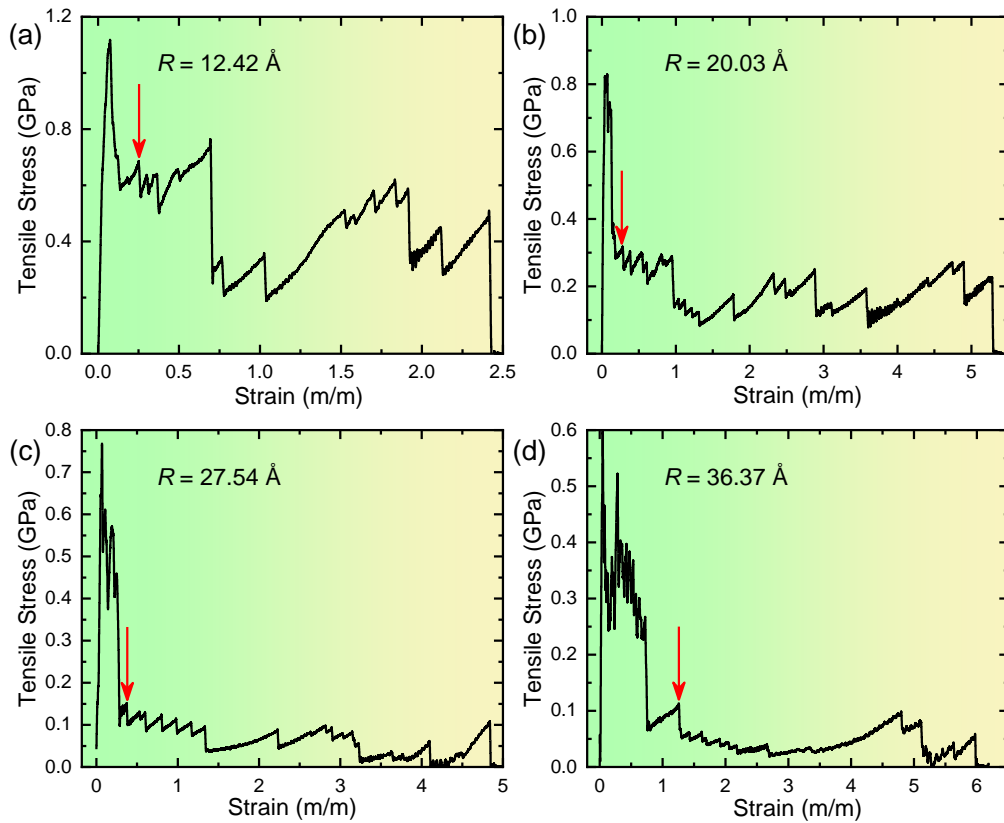
Figure 5. Global tensile mechanical stress-strain responses of 3D spirally wound MoS2 nanostructures with outer coiled radius of (a) $R = 12.42$ Å, (b) $R = 20.03$ Å , (c) $R = 27.54$ Å  and (d) $R = 36.37$ Å, respectively. All studied $MoS_2$ spirals show strong nonlinearity in the loading curves, indicating complex structural transformations inaccessible from conventional engineering springs. Mechanical properties of those $MoS_2$ spirals including initial stiffness, maximum tensile strength, elastic strain and rupture strain are dimensionality dependent. The red arrows in the curves indicate the critical strains, above which $MoS_2$ spirals are catastrophically failed via dissociation of the strong covalent bonds of Mo-S.
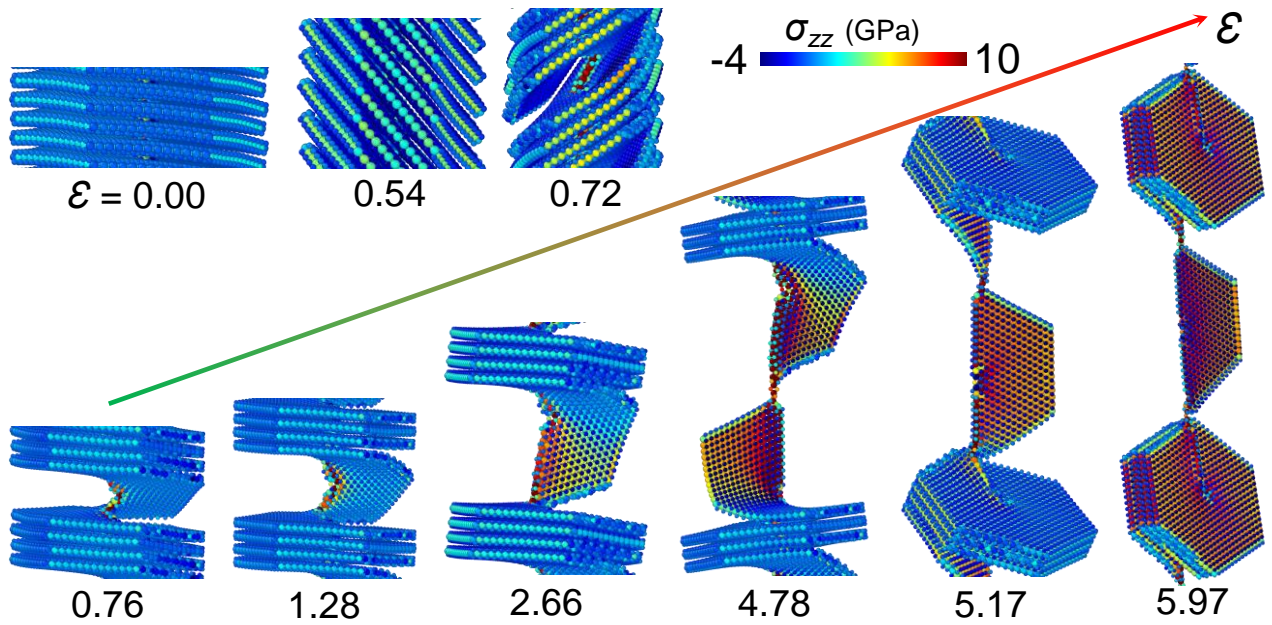
Figure 6. Development of molecular structure of non-hollow $MoS_2$ spiral with outer radius of 36.37 Å subjected to helical axial tension. A series of side-viewed snapshots of helical configurations of the $MoS_2$ spiral at different tensile strains are shown to reveal the deformational characteristics, where the color code is based on the tensile stress $\sigma_{zz}$. The $MoS_2$ spiral shows very complex deformational mechanisms. Within strain from 0.00 to 1.28, sliding, reorientation, buckling and opening mainly dominate the elastic deformations. It is observed that only one coiled nanoribbon is opened to accommodate the limit elastic strain. Beyond the elastic strain of 1.28, plastic deformations by break-vs-arrest events take place in the inner hexagon-corner to separate the partial opened $MoS_2$ spiral.
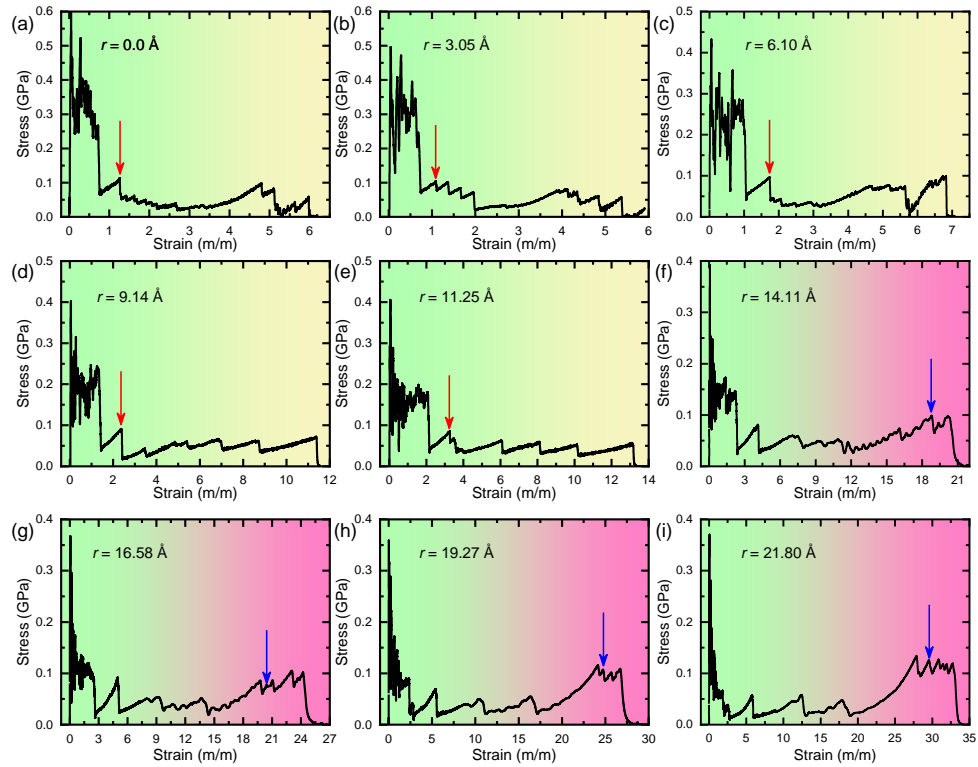
Figure 5. Complete stretching mechanical stress-strain diagrams of 3D spirally wound $MoS_2$ nanostructures with inner coiled radius of (a) $r = 0.00$ Å, (b) $r = 3.05$ Å , (c) $r = 6.10$ Å, (d) $r = 9.14$ Å, (e) $r = 11.25$ Å, (f) $r = 14.11$ Å , (g) $r = 16.58$ Å, (h) $r = 19.27$ Å and (i) $r = 21.807$ Å, respectively. Independent on the inner radius, all investigated $MoS_2$ spirals exhibit characteristic sawtooth-like patterns in the stretching curves. The initial steep increases in loading stress primarily come from the vdW interaction between coiled nanoribbons of $MoS_2$ spirals. The subsequent frequent oscillations in the loading stress are mainly attributed by the sliding-reorientation-buckling deformation mechanisms. The red and blue arrows in the curves indicate the critical strains, above which catastrophic failure of $MoS_2$ spirals occurs via breaking the covalent bonds of Mo-S. Intriguingly, a critical inner radius between $r = 11.25$ Å and 14.11 Å that strongly affects the elasticity is identified, resulting from distinct elastic deformation mechanisms.
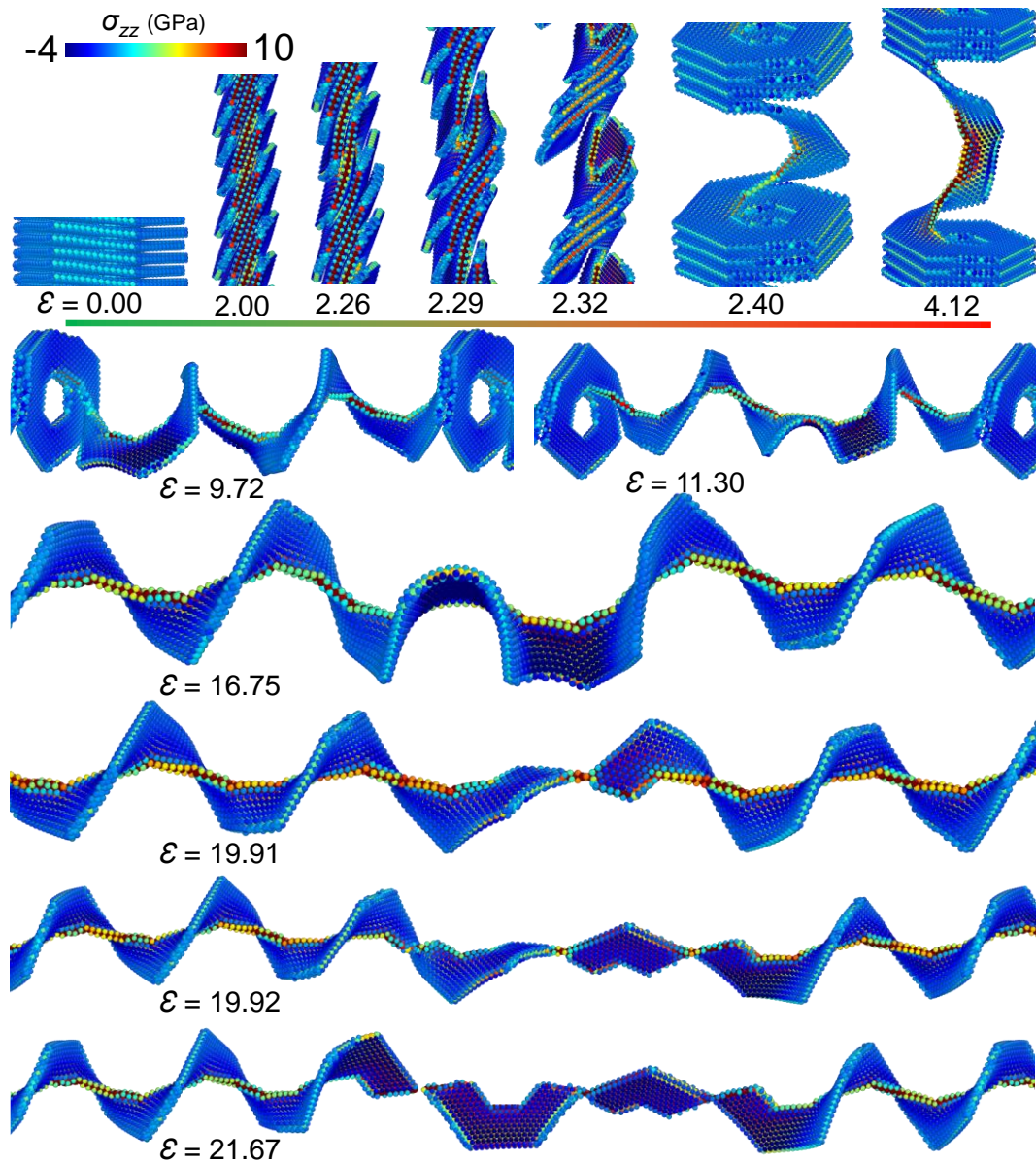
Figure 6. Molecular structural evolution of hollow $MoS_2$ spiral with inner radius of 11.41 Å under helical axial tension. Numbers of side-viewed snapshots of coiled configurations of the $MoS_2$ spiral at different strain levels are captured to uncover the supergiant deformation characteristics. Within the initial elastic strain region of about 0.00 to 4.12, this $MoS_2$ spiral presents the similar elastic deformation characteristics to that of non-hollow $MoS_2$ spirals. Note that the large elasticity in this region comes from large sliding displacements between coiled nanoribbons. In the intermediate elastic tension stage (from around 4.12 to 16.75), the surpergiant elastic deformation is characterized by the sliding, buckling and the stepwise opening of all coiled nanioribbons. It is observed that one

coiled nanoribbon with unique morphology from other coiled ones is severely buckled. The late elasticity is dominated by elastic stretching of opened coiled nanoribbons. As exceeding the supergiant elastic strain of around 19.90, plastic deformations is analogously characterized by multiple breaking-vs-arresting of Mo-S bonds located at the inner hexagon-corner of the highly elongated $MoS_2$ spiral.